# Supporting Information

Terahertz deep-optics imaging enabled by perfect lens-initialized optical and electronic neural networks

Ping Tang[1], Wei Wei[1], Borui Xu[1], Xiangyu Zhao[1], Jingzhu Shao[1], Yudong Tian[1], Chongzhao Wu[1] *

[1] Author address: Center for Biophotonics, Institute of Medical Robotics, School of Biomedical Engineering, Shanghai Jiao Tong University, Shanghai, 200240, China

* E-mail: czwu@sjtu.edu.cn
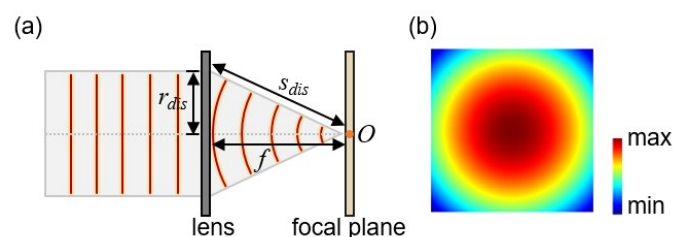
Figure S1. Modulation principle of conventional refractive lens. (a) Illustration of refractive lens for beam focusing, where the red lines denote the wave fronts, the grey dotted line indicates the optical axis, s_{dis} indicates straight-line distance between the edge position on lens and the focal point, r_{dis} denotes the radial distance from the edge point to central optical axis, f is the focal length, point O denotes the focal point; (b) the corresponding phase profile of refractive lens, where "min" and "max" specify the range of the absolute phase shift.
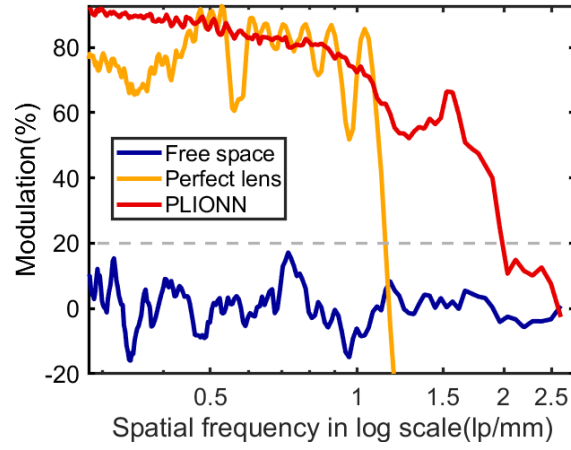
Figure S2. Modulation transfer function (MTF) curves on Siemens star chart utilizing free space propagation, conventional refractive lens and perfect lens-initialized optical neural network (PLIONN), respectively, where the grey dotted line indicates the cutoff frequency.
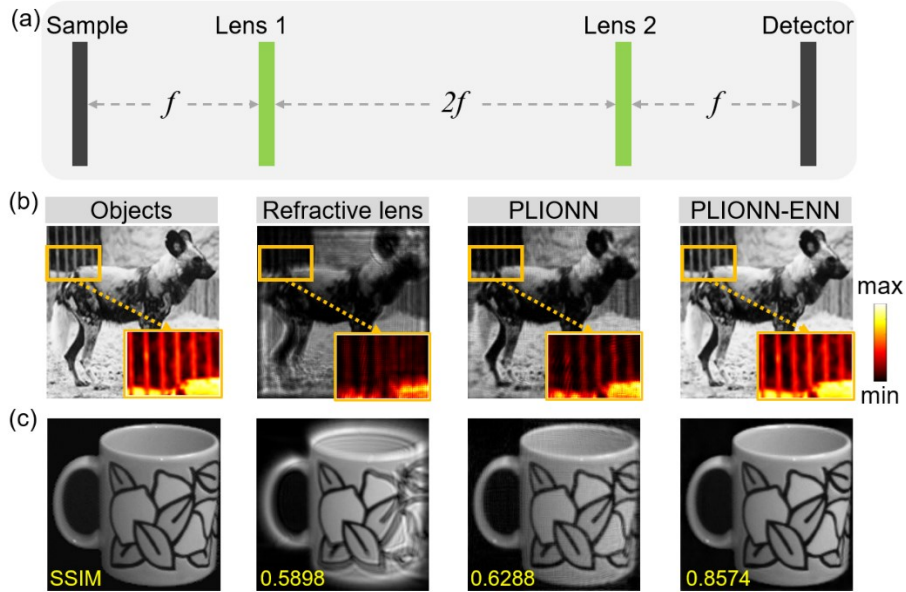
Figure S3. (a) Schematic illustration of a 4f conjugate system, where f denotes the focal length, (b)-(c) imaging results using conventional refractive lenses, PLIONN model and PLIONN-ENN model in the 4f conjugate system on ImageNet dataset and COIL-100 dataset, respectively.
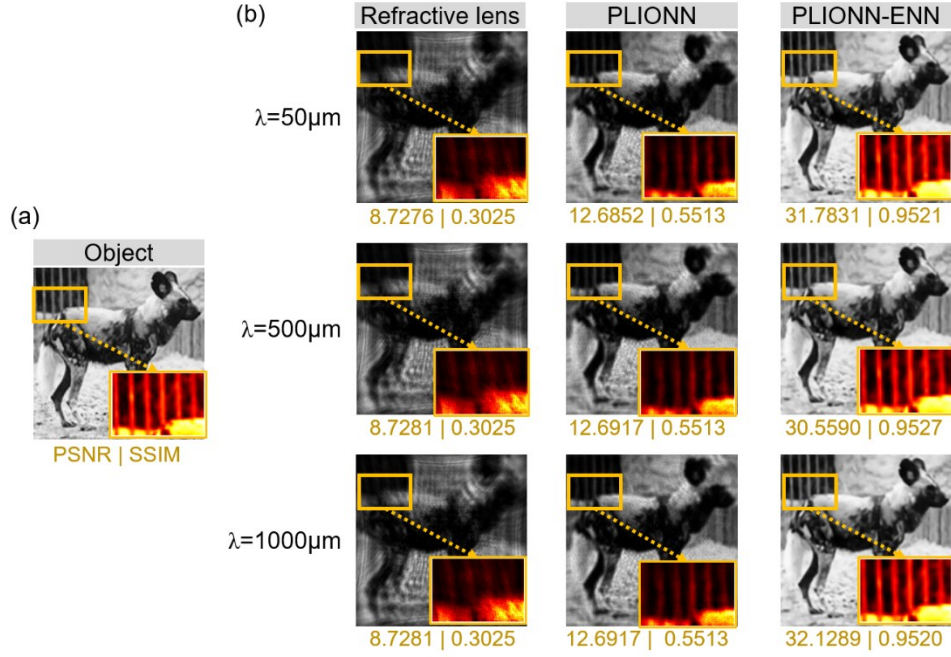
Figure S4. (a) Imaging object, (b) imaging results for working wavelength of λ=50μm, 500μm and 1000μm, respectively, using conventional refractive lenses, PLIONN model and PLIONN-ENN model, in terms of PSNR and SSIM metrics.

Supporting section A: Training steps of the PLIONN model

The training process of our perfect lens-initialized optical neural networks (PLIONN) is similar to that of electronic neural networks, as illustrated in Figure S5. The corresponding description for the detailed training steps is as follows:

Step 1. Initialize the phase shift of the neurons in diffractive layers with the lens phase profile according to Equation (1) in the manuscript.

Step 2. Randomly select training samples from the training set in ImageNet dataset.

Step 3. Simulate the process where the incident light forward propagates through the sample and diffractive layers to reach the detector and generate the imaging result, according to Equations (2)-(4) in the manuscript. During this process, the phase shifts of neurons in the diffractive layers are fixed and not updated, as indicated by the gray circles in Figure S5.

Step 4. Calculate the error between the imaging results from *Step 3* with the ideal imaging objects (i.e. the training sample in *Step 3*) using Equation (5) in the manuscript.

Step 5. Back propagate the error from the detector layer through the diffractive layers to the sample layer, compute the gradients of the error against each neuron, and optimize the phase modulation parameters of the neurons in the direction of gradient descent, as indicated by the orange circles in Figure S5.

Step 6. Repeat *Steps 2-5* above until the error reaches a minimum or satisfying the maximum number of iterations. The final phase modulation parameters are then frozen and taken as the modulation parameters of a well-trained PLIONN model.
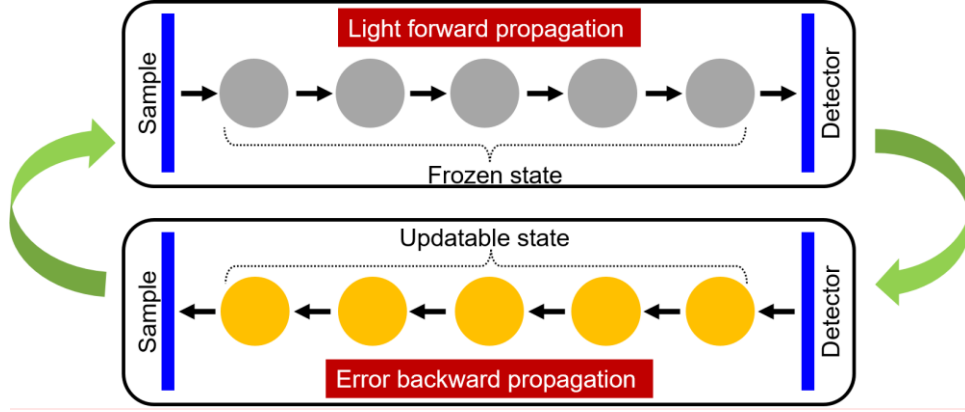
Figure S5. Illustration of the training procedure of PLIONN model, where the gray and orange circles represent neurons in each diffractive layer, with each neuron functioning as a local phase modulation unit. Gray circles indicate neurons with frozen phase modulation parameters, while orange ones indicate those with updatable parameters.

Supporting section B: About zero-amplitude padding

Assuming the wave vector k of a plane wave lies within the xz-plane and the z-axis serves as the principal optical axis of imaging system, according to angular spectrum theory, its spatial frequency u is closely related to the propagation divergence angle θ, and can be expressed as follows:

$$u = \frac{1}{d} = \frac{\sin\theta}{\lambda}$$

(S1)

where d is the spatial period, and λ is the wavelength of light, as illustrated in Figure S6, where the wave vector with higher spatial frequency (i.e. u_2) correspond to a larger divergence angle (i.e. θ_2). Consequently, fine-grained features tend to propagate at larger divergence angles, making them more likely to fall outside the receiving area of

subsequent optical elements, leading to the loss of sample information. In contrast, uniform features typically propagate along the principal optical axis, resulting in less information loss.

Therefore, in order to reproduce the fine structures of the imaging sample more accurately, zero-amplitude padding is introduced and applied around the sample. By making the diffractive layers slightly larger than the sample, more high-frequency information from the sample can be captured, thereby enhancing the spatial resolution. In this study, the side size of zero-amplitude padding region is set as 56 pixels.
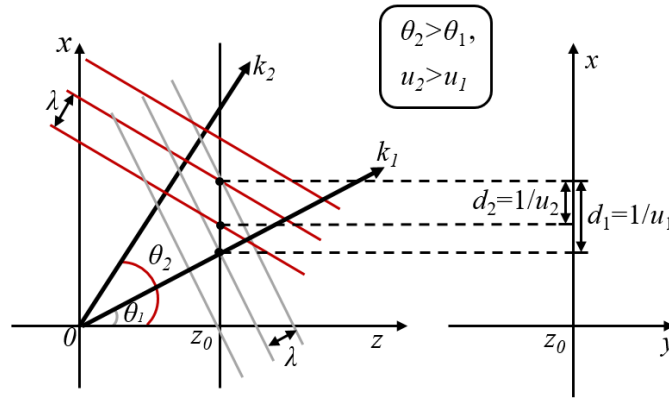
Figure S6. Schematic illustration of the divergence angle θ and spatial frequency u of the propagation waves, where the z-axis is the main optical axis, k is the wave vector in the xz plane, λ is the wavelength of the light, and d represents the spatial period (reciprocal to the spatial frequency u), the clusters of gray and red lines represent the isophase lines corresponding to wave vectors k_1 and k_2, respectively.

Supporting section C: Physical implementation of PLIONN model

Current literatures usually utilize 3D printing technology to fabricate diffractive layers in phase-only optical neural networks (ONNs) [S1, S2] as diffractive optical elements (DOEs), where the phase shift φ of each neuron in diffractive layers is linearly transformed into the height h of the unit in DOE by the following formula:

$$\varphi = \frac{2\pi}{\lambda} \Delta n_{eff} h \tag{S2}$$

where λ denotes the working wavelength, Δn_{eff} the difference of the effective index between the 3D printing material and the air. However, due to the limitation in printing precision and resolution, this technology is more suitable for long operating wavelength, such as 750μm, 0.4THz in Ref. [S1], with a larger geometry for a higher error tolerance. Moreover, the printed DOEs usually face the challenges related to high-order diffraction and low spatial utilization since the scale of neurons in diffractive layers is comparable to their working wavelength.

According to Rayleigh criterion and the related diffractive theory, the shorter the wavelength, the higher the imaging resolution. Considering this, our work focuses on a shorter wavelength, such as λ=116μm for a naturally higher spatial resolution. Therefore, the commonly-used 3D printing technology is no longer applicable in this work. As a solution, a better way to physically implement the proposed PLIONN model is to employ geometric phase (also called Pancharatnam-Berry phase) coded metasurfaces [S3, S4]. Similar to the linear transformation between the phase shift and the unit height in 3D printing technology, geometric phase-based metasurfaces control the phase shift φ of a specific unit cell by adjusting its rotation angle θ, i.e.

$$\varphi = 2\alpha\theta \tag{S3}$$

where $\alpha = \pm 1$ is a sign corresponding to right-circularly polarized (RCP) or left-circularly polarized (LCP) incident waves. Considering the availability of materials and processing technology, the high-resistivity, single-crystal float-zone silicon serves as the substrate and our PLIONN model is implemented as the cascaded all-silicon metasurfaces, which can be fabricated by reactive ion etching technology. Detailed descriptions are as follows.

Figure S7(a) presents the schematic diagram of the designed all-silicon rectangular unit cell, where l, w, and h represent the length, width, and height of the unit cell, respectively, θ the rotation angle around the center of the unit cell, p is the period of unit cell and set as half of the wavelength, i.e. p=58 μm, to match the side length of the neuron in PLIONN. Since the size of unit cells is smaller than the working wavelength,

the proposed metasurface can offer higher spatial neuron density while eliminating the impact from high-order diffraction.

Firstly, in order to determine the geometric dimensions of the unit cell, commercially-available software Lumerical finite-difference time-domain (FDTD) is adopted to obtain the amplitude transmittance for each pair of the dimensions, where length l and width w range from 10 to 50 μm, respectively, height h is uniformly set at 70 μm (a tradeoff between modulation capability and experimental fabrication). Moreover, the refractive index of silicon substrate for the chosen wavelength (λ=116μm) is set as 3.418 and the absorption coefficient as about 0.0004 mm^{-1} according to Ref. [S5]. The corresponding simulation results are shown in Figure S7(b), according to which we specify the length l as 44μm and the width w as 21μm to achieve both a higher amplitude transmittance and a higher phase modulation efficiency, as indicated by the blue star symbol pointed by the blue arrow in Figure S7(b).

Based on the selected unit cell, Lumerical FDTD is adopted again to check the influence for modifying the rotation angles. As shown in Figure S7(c), the amplitude transmittance remains the same for both left-circularly polarized (LCP) and right-circularly polarized (RCP) incident light. Meanwhile, the phase shift and rotation angle closely adhere to Equation (S3), with an inverted phase shift exactly corresponding the 180° phase difference between LCP and RCP. Then the phase shift of each neuron in PLIONN model can be mapped as the rotation angle of the unit cell. Figure S7(d) shows a schematic view of the generated cascade metasurfaces, where the red and yellow insets denote the magnified plot for the selected region.
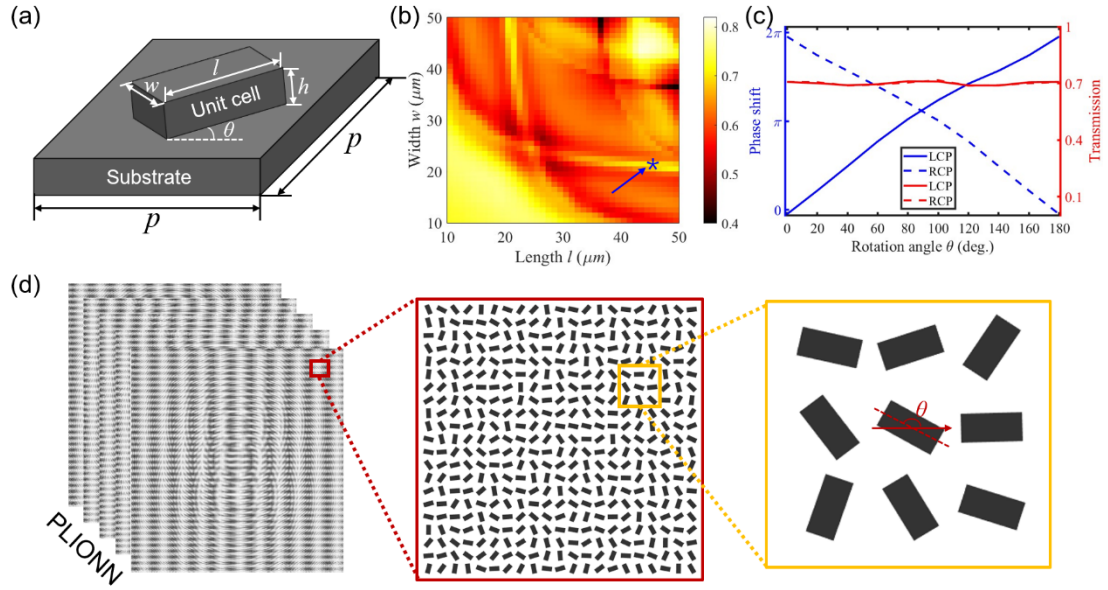
Figure S7. Physical implementation of PLIONN model by geometric phase coded metasurfaces. (a) Three-dimensional schematic view of the unit cell in all-silicon metasurface, where l, w, h denotes the length, width, and height of unit cell, respectively, and θ the rotation angle, p the period. (b) Transmittance distribution of unit cell corresponding to different length l and width w, while remaining h =70μm, p=58μm and θ=0°, where the blue star pointed by the blue arrow indicates the selected geometry. (c) Phase shift and amplitude transmittance with respect to rotation angle θ for incident light with left-circularly polarization (LCP) and right-circularly polarization (RCP), respectively. (d) Schematic top view of the physical PLIONN model consisting of cascaded metasurfaces, where the red and yellow insets denote the magnified plot for the selected region (For a better visualization, substrate beneath the unit cell is not shown).

To more accurately simulate real imaging scenarios, the impact of potential fabrication errors (i.e. the etching errors) on the imaging quality of both PLIONN and PLIONN-ENN models is additionally estimated, as shown in Figure S8. From Figure S8(a), it can be observed that the imaging quality of PLIONN model, indicated by metric SSIM, continuously decreases with the increasing of fabrication errors. The SSIM value reaches the lowest at 10% error, corresponding to an intuitive imaging

presented in Figure S8(d), while Figures S8(b)-(c) represent the imaging target and the ideal imaging without fabrication error of PLIONN model, respectively.

It is also evident that the PLIONN-ENN model maintains a high performance despite the increasing of fabrication errors, as indicated by the red dotted line in Figure S8(a). Furthermore, although the imaging in Figure S8(d) suffers from noise and low contrast, the texture details remain clearly preserved, as illustrated in the yellow inset of Figure S8(d), and can be accurately reconstructed by the subsequent ENN model, as demonstrated in Figure S8(e). Thus, it can be concluded that as an integrated optoelectronic system, the process of ENN model is able to effectively mitigate the impact of fabrication errors on PLIONN model, ensuring that the overall system maintains high imaging quality and robustness.
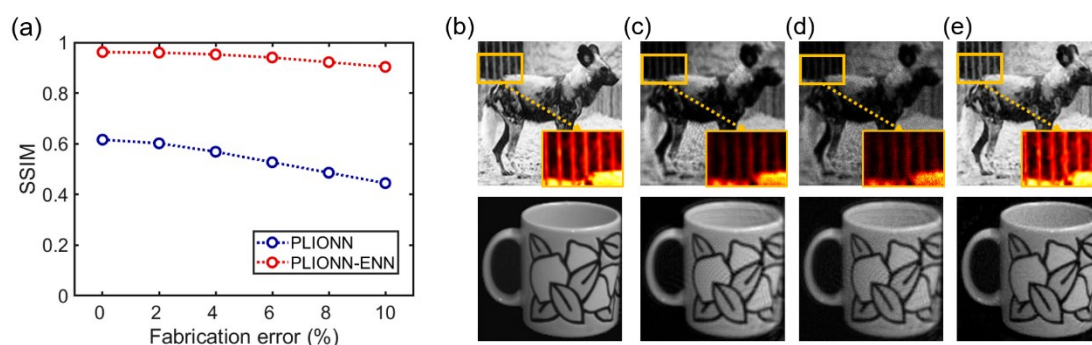
Figure S8. Simulation on fabrication error. (a) Imaging quality in terms of SSIM for different level of fabrication errors in PLIONN and PLIONN-ENN systems on ImageNet dataset, (b) imaging target, (c) imaging results by ideal PLIONN without fabrication error, (d) imaging results by PLIONN with 10% fabrication error, and (e) imaging results by PLIONN-ENN with 10% fabrication error.

The physical PLIONN imaging system can be constructed as Figure S9. An off-axis parabolic mirror (OAPM) is equipped to collimate the emitting beam from the laser source, while a linear polarizer (LP) and a quarter-wave plate (QWP) are used to control the polarization of the incident beam and generate circularly polarized waves required by the following geometric-phase metasurfaces. Then the incident waves pass through the imaging sample, get modulated by the metasurfaces, i.e. the PLIONN model, finally captured by the detector. Moreover, it is notable that to deal with the large imaging area

in detector layer (400×400 pixels, approximately 2.3×2.3 cm), a two-axis translation stage has been integrated into the imaging system to facilitate the detection process. For instance, the single-pixel detector or array detector can be mounted on the translation stage for point-by-point [S1] or region-by-region [S6] imaging, as indicated by the pink half frame in Figure S9, or conversely, the sample and diffractive layers are mounted and moved on the translation stage while keeping the location of the detector fixed [S7], as indicated by the green half frame in Figure S9."
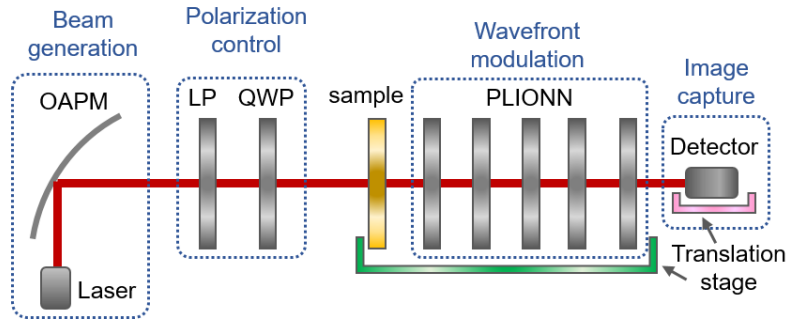
Figure S9. Optical path diagram for the PLIONN imaging model, where PLIONN is composed of the cascaded geometric-phase metasurfaces, OAPM denotes the off-axis parabolic mirror, LP the linear polarizer, QWP the quarter-wave plate, the pink and green half frame indicate the either location of the translation stage.

The above implementation of PLIONN model by geometric-phase metasurfaces is straightforward enough. However, such approach requires the extra polarization components in the optical path, as shown by the polarization control module in Figure S9. Another way to physically implement PLIONN model is to employ transmission-phase metasurface. Instead of manipulating the rotation angles, transmission-phase metasurfaces perform phase modulation by continuously adjusting the geometric dimensions of the unit cells, i.e. the length l and width w, as illustrated in Figure S10(a). Then we adopt Lumerical FDTD software to acquire the detailed relationship between the phase shifts and the geometric dimensions, where length l and width w of the unit cell gradually increase from 14μm to 54μm, while the height h of the cuboid unit cell is fixed at 70μm and the period p is 58μm. The corresponding amplitude transmittances as well as the phase shifts are illustrated in Figure S10(b)-(c), which serve as the

geometry database for the following implementation. According to the length/width-amplitude/phase maps in Figure S10(b)-(c), nearly arbitrary phase shifts from 0 to 2π with a high amplitude transmittance can be simultaneously obtained through carefully choosing length and width of the unit cell from the database, as shown by Figure S10(d). It can be observed that when the amplitude transmittance is controlled around 60%, there are over 6,000 pairs of geometry parameters located between [0, 2π], which fully satisfies the requirement for continuous phase modulation across the entire range. Then the PLIONN model can be easily experimentally demonstrated by selecting the unit cells from the database according to the phase shift of neurons. A partial schematic layout of the PLIONN model as transmission-phase metasurfaces is presented in Figure S10(e), showing varied lengths and widths corresponding to each phase shift. This way of implementation does not require the polarization control of the incident light, thereby simplifying the imaging optical path, as depicted in Figure S10(f).
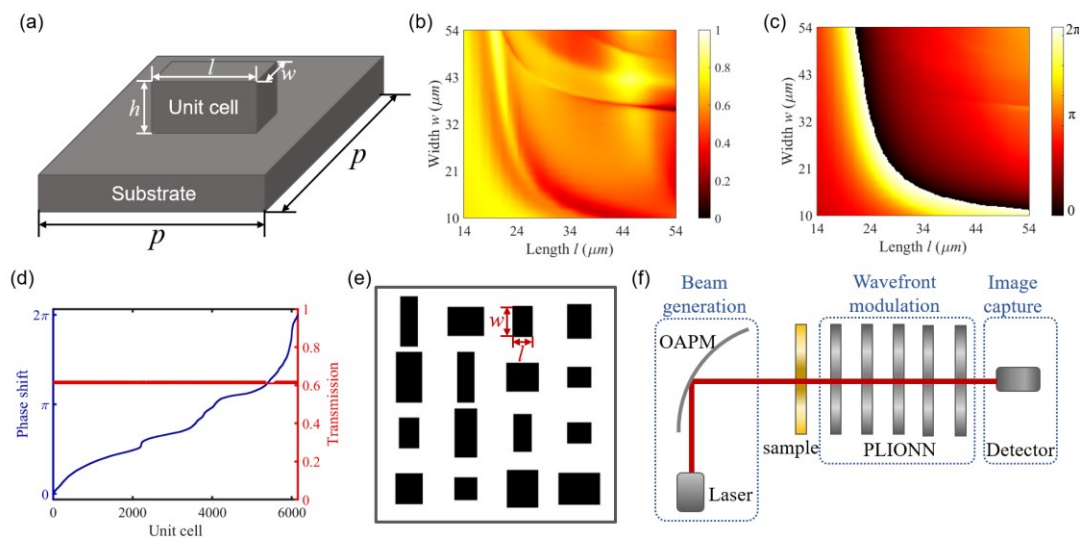
Figure S10. Physical implementation of PLIONN model by propagation-phase metasurface. (a) Three-dimensional schematic view of the unit cell for propagation phase in silicon substrate, where l, w, h denotes the length, width, and height of unit cell, respectively, and θ the rotation angle, p the period. (b)-(c) Transmittance and phase shift distribution of unit cell corresponding to different length l and width w, while remaining h =70μm and p=58μm. (d) Transmittance and phase shift with respect to rotation angle θ for incident light with LCP and RCP, respectively. (e) The magnified

plot of PLIONN consisting of unit cells. (f) The corresponding schematic optical path diagram for PLIONN imaging system, where OAPM denotes the off-axis parabolic mirror.

As has been discussed, in terms of fabrication at a shorter wavelength range in terahertz bands targeting at a higher resolution of the imaging, the commonly-used 3D printing technology is no longer applicable. As a solution, a better way to physically implement the proposed PLIONN model is to employ all-silicon geometric phase coded metasurfaces or transmission-phase metasurfaces, which can be fabricated by standard photolithography and deep dry etching technique. Considering the attenuation of the incident terahertz wave through multiple diffractive layers, i.e. multiple cascaded metasurfaces, it is ideal to utilize higher-power gas laser or free-electron laser, as the terahertz light source of the system. However, due to the large size and expensive cost of such sources, compact terahertz quantum cascade lasers (THz QCLs) covering the lasing frequency from ~ 2 THz to 5 THz are able to serve as the source for the initial experimental setup to demonstrate that the fabrication and light modulation capability of the all-silicon metasurface with designed unit cells at the given wavelength (λ=116μm in the manuscript) are feasible, which are significantly crucial in the physical implementation scheme for our PLIONN model. Limitations include the low output power from THz QCLs, sensitivity of available THz camera and further attenuation in intensity of the incident terahertz wave by imaging samples. Similar implementations have been demonstrated in recent researches. For example, Jiang et al. [S8] proposed and successfully fabricated an all-silicon geometric phase coded metasurface at a working wavelength of 118.8 μm for sub-diffraction focusing and long-depth imaging. Similarly, in [S9], Wang et al. designed a high numerical aperture square all-silicon metalens at 118.83μm by hybridizing the transmission phase- and the geometric phase-coded metasurfaces. More recently, Liu et al. [S10] physically mapped the optical neural network as cascade silicon metasurfaces coded by transmission phase and has successfully applied it for optical logic operation. These researches, either adopting similar structural units and working wavelengths or employing the same

implementation scheme (i.e. cascaded metasurfaces), can provide valuable references for the physical implementation of our proposed model.

Moreover, since each diffractive layer in PLIONN model contains 512×512 pixels (about 3×3 cm) and the typical size of silicon substrates being around 1mm, the PLIONN model can be physically regarded as a series of special flat lenses with each component size of less than 3×3×0.1 cm, which would also promote the development of ultra-thin devices for terahertz imaging.

**Supporting section D: Imaging with non-uniform incident light**

Considering that the terahertz beam illuminating on imaging targets is often non-uniform in practice, we take the more commonly-used Gaussian-shape beam [S11,S12], instead of the default ideal plane waves, as the instance to evaluate the performance of our perfect lens-initialized optical neural network (PLIONN) and electronic neural network (ENN) in the case of non-uniform incident light. The imaging results with Gaussian-shape incident light are presented in Figure S11, where an obvious increase of PSNR and SSIM can be observed from the conventional refractive lens to PLIONN and to PLIONN-ENN, even with different beam width, demonstrating the superiority of the proposed PLIONN(-ENN) over the conventional lens.
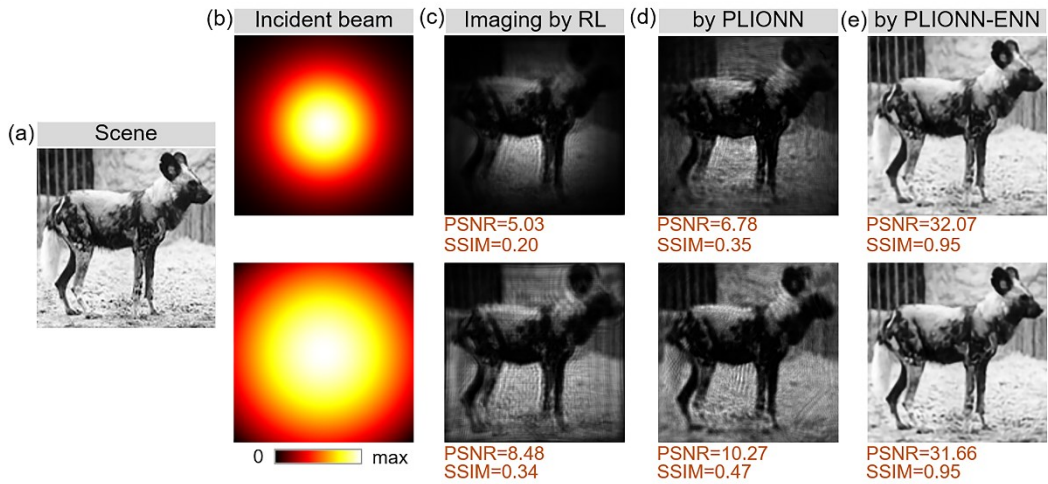
Figure S11. (a) the imaging target, i.e. the scene, (b) the cross-sectional distribution of Gaussian-shape incident light, (c)-(e) imaging results using a single refractive lens (RL), PLIONN, and PLIONN-ENN, respectively.

Supporting section E: Imaging with tunable magnification

Considering that the size of imaging targets and detection area may not exactly match, we explored zoom-in (2× magnification as an example) and zoom-out (0.5× magnification as an example) imaging using the PLIONN-ENN model as well. In actual imaging scenarios, zoom-in imaging can capture the details of objects more clearly, while zoom-out imaging can reduce the detection area and improve the imaging speed (especially for point-by-point scanning). According to the Gaussian form of thin-lens equation, the zooming is achieved by adjusting the object distance and image distance, i.e. the distance from the imaging targets to the first diffractive layer and from the last diffractive layer to the detector. It is worth noting that an extra residual block for up-sampling is added in the ENN model for the equal-size restoration. Results in Figure S12 confirm that the proposed PLIONN(-ENN) model is flexible enough to deal with the mismatched size of objects and detector, which also indicates its potential for the advanced applications, such as microscopy and compressed imaging.
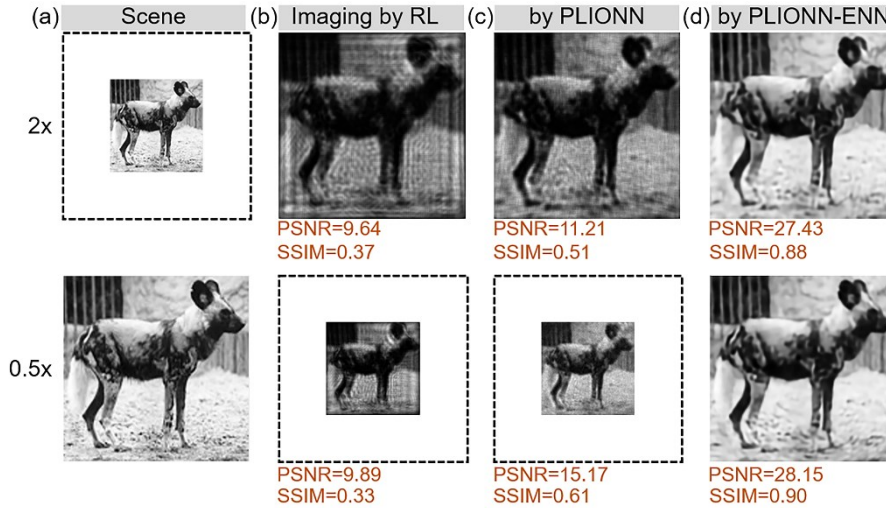
Figure S12. (a) the imaging targets, i.e. the scenes, (b)-(d) imaging using a single refractive lens (RL), PLIONN, and PLIONN-ENN, respectively, where 2× and 0.5× denote the magnification times.

Supporting section F: Far-field and broadband chromatic imaging

The proposed model in manuscript is based on the situation that the object distance is finite, which is also the default setting throughout our work. However, when distance between the imaging target and the lens is infinite, angular spectrum method may not applicable anymore and the light propagating onto the lens can be treated as parallel beams. Considering this, an image degradation model is incorporated into the proposed PLIONN model to deal with the case of infinite object distance. The degraded image I_{deg} can be regarded as the convolution of the imaging target I_{tar} and the point spread function (PSF) ρ, and formulated as:

$$I_{\deg}\left(x,y\right) = I_{tar}\left(x,y\right) * \rho\left(x,y\right) + \eta\left(x,y\right) \tag{S4}$$

where * represents the 2D spatial convolution operator and η denotes the system noise. For this special case of infinite object length, PSF is calculated by placing a point source at the object plane and capturing the propagated light waves from the point source through the PLIONN to the detector, as illustrated in Figure S13(a).

Moreover, due to the dispersion effect, imaging systems with refractive lenses intrinsically suffer from chromatic aberrations, where the spatial position of the focal point deviates with the incident wavelength, thereby severely degrading the imaging quality. In the above evaluation, we aim at monochrome imaging with grey-value objects for the sake of simplicity. In fact, the proposed PLIONN-ENN model also has great potential in achromatic multi-wavelength imaging. Here we demonstrate the correction for chromatic aberration of the proposed model in case that the object distance is infinite (assuming that the PSF is spatially invariant), where the system noise η is modeled as Gaussian distribution with the mean value μ set as μ=0 and standard deviations σ set as σ=0.1 by default. Figure S13(b)-(d) presents the pseudo-color images using refractive lens, PLIONN and PLIONN-ENN models, respectively. These colorful images are synthesized from three different wavelengths (λ=26 μm, 116 μm and 206 μm, almost covering the entire THz band) while the imaging target is shown in Figure S13(e). Both the narrower PSFs and the increasing SSIMs confirm the achromatic

ability of the proposed PLIONN(-ENN) model. Moreover, a stepwise correction in terms of SSIM is given in Figure S13(f), further validating its powerfulness and robustness in broadband achromatic imaging. In addition to the results mentioned above, the impact of larger standard deviation σ, i.e. more severe system noise, on imaging quality was also explored. As demonstrated in Figure S13(g), when the standard deviation of Gaussian noise model increases to σ=0.5, the PSF can still be accurately optimized. However, the imaging results from refractive lens and PLIONN model suffer from more significant degradation, with lower SSIM values. Fortunately, the performance of subsequent ENN model is robust enough to substantially mitigate the impact of system noise, enabling high-quality reconstruction of noise-polluted images captured by the optical module.
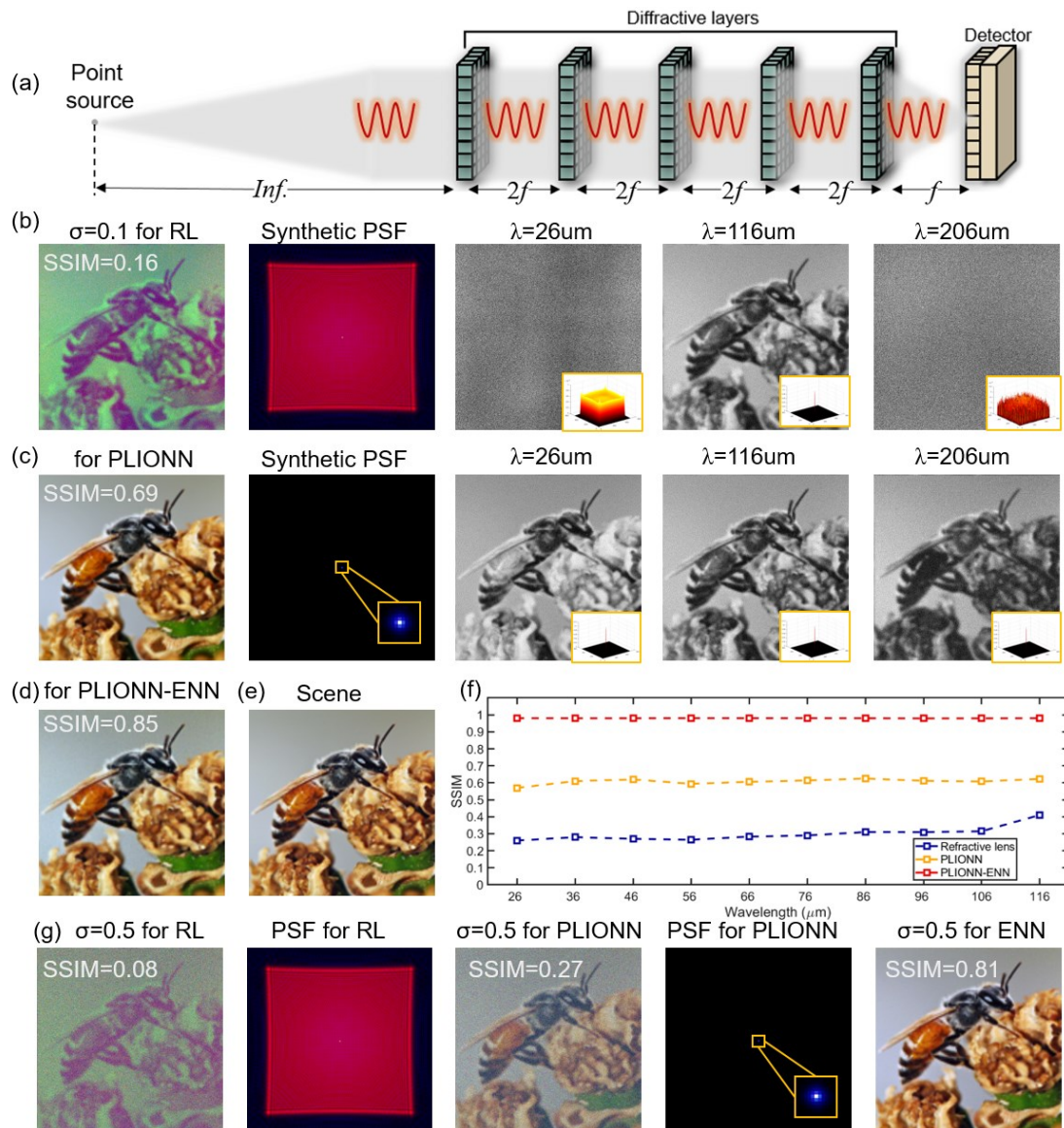
Figure S13. (a) Modeling of the point spread function (PSF) for imaging targets at infinity, in which light waves from the point source propagate through the PLIONN and get captured by the detector. f represents the focal length of perfect lens utilized for phase initialization, (b)-(d) multi-wavelength imaging using a single refractive lens (RL), PLIONN and PLIONN-ENN, respectively, where insets in yellow boxes denote the PSF for each wavelength, and the standard deviation σ of Gaussian noise model set as σ=0.1, (e) the imaging target, (f) the stepwise correction for chromatic aberration, (g) imaging when the standard deviation σ of Gaussian noise model increases to σ=0.5.

Supporting section G: Imaging with physics-driven convolutional neural network

Inspired by our previous work [S13], a more complicated physics-driven convolutional neural network is developed in this section to design the phase profile φ of each diffractive layer in optical neural network (ONN). The architecture is presented in Figure S14(a), where I_{in} and I_{out} indicate the light intensity in object plane and imaging plane, f_{enc} and f_{dec} represent the encoder and decoder in [S3], respectively. Each pair of encoder and decoder is used to generate the phase profile φ in one diffractive layer. Considering the limited computational resources, all the decoders share the same encoder. f_{asm} denotes the function for angular spectrum method, f_{hyb} the hybrid of multiple operations, and f_{mode} the function for mode calculation, defined as:

$$M_0 = f_{asm}\left(I_{in}\right) = F^{-1}\left(F\left(I_{in}\right) \cdot H\right) \tag{S5}$$

$$M_{i+1} = f_{hyb}\left(M_i, \varphi_{i+1}\right) = F^{-1}\left(F\left(M_i \cdot e^{j\varphi_{i+1}}\right) \cdot H\right) \tag{S6}$$

$$I_{out} = f_{mode}\left(M_k\right) = \left|M_k\right|^2 \tag{S7}$$

where M denotes the intermediate variable of light field, $F(.)$ and $F^{-1}(.)$ denote Fourier and inverse Fourier transform, respectively, H is the transfer function, i is an integer ranging in $[0, k]$, k denotes the number of diffractive layers. Unlike the proposed PLIONN, phase profiles derived from the physics-driven convolutional neural network

are image-specific, and therefore for different imaging targets, the network generates different profiles.

As intuitively shown in Figure S14(b), a high imaging quality has been demonstrated when using ONN designed with physical drive convolutional neural network for imaging, with more edge and texture details preserved. And statistically, the average PSNR is 35.99 and SSIM is 0.93, which is much better than that of PLIONN (13.24 for PSNR and 0.62 for SSIM) and even comparable to PLIONN-ENN (33.56 for PSNR and 0.96 for SSIM), indicating almost the best an optical system can achieve individually in the domain of high-quality imaging. More importantly, the above results reveal the strong potential of deep electronic neural networks in optimizing ONNs, which may provide a new insight to rescue ONN from the urgent thirst for non-linear materials and facilitate the high performance of ONN in a broad range of applications.
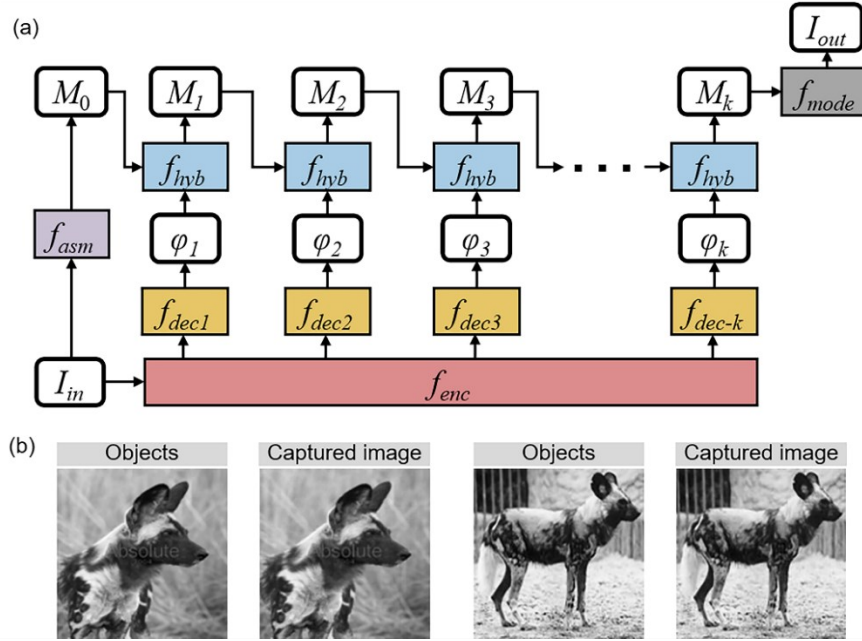
Figure S14. (a) Structure of the physics-driven convolutional neural network for the design of ONN, (b) objects and the corresponding imaging results when $k=5$.

Supporting References:

[S1] X. Lin et al., "All-optical machine learning using diffractive deep neural networks," Science, vol. 361, no. 6406, pp. 1004-1008, 2018.

[S2] M. Rahman et al., "Computer-free, all-optical reconstruction of holograms using diffractive networks," ACS Photonics, vol. 8, pp. 3375-3384, 2021.

[S3] E. Hasman et al., "Polarization dependent focusing lens by use of quantized Pancharatnam-Berry phase diffractive optics," Appl. Phys. Lett. vol. 82, pp. 328–330, 2003.

[S4] D. Lin et al., "Dielectric gradient metasurface optical elements," Science, vol. 345, pp. 298–302, 2014.

[S5] J M Dai et al., "Terahertz time-domain spectroscopy characterization of the far-infrared absorption and index of refraction of high-resistivity, float-zone silicon," J. Opt. Soc. Am. B, vol. 21, pp. 1379–1386, 2004

[S6] Z. Y. Li et al., "Terahertz synthetic aperture in-line holography with intensity correction and sparsity autofocusing reconstruction," Photon. Res., vol. 7, pp. 1391-1399, 2019.

[S7] Y. Y. Zhang et al., "Continuous-wave THz imaging for biomedical samples," Appl. Sci., vol.11, no. 71, 2021.

[S8] X. Jiang et al., "All-dielectric metalens for terahertz wave imaging," Opt. Express, vol. 26, no. 11, pp. 14132-14142, 2018.

[S9] Z. W. Wang et al., "A high numerical aperture terahertz all-silicon metalens with sub-diffraction focus and long depth of focus," Phys. D: Appl. Phys., vol. 54, no. 085103, 2021.

[S10] Y. F. Liu et al., "All dielectric metasurface based diffractive neural networks for 1-bit adder," Nanophotonics, vol. 13, no. 8, pp. 1449-1458, 2024.

[S11] B. Recur et al., "Terahertz radiation for tomographic inspection," Opt. Eng., vol. 51, no. 9, pp. 091609, 2012.

[S12] B. Recur et al., "Ordered subsets convex algorithm for 3D terahertz transmission tomography," Opt. Express, vol. 22, no. 19, pp. 23299-23309, 2014.

[S13] W. Wei, P. Tang, J. Shao, J. Zhu, X. Zhao, and C. Wu, "End-to-end design of metasurface-based complex-amplitude holograms by physics-driven deep neural networks," Nanophotonics, vol. 11, no. 12, pp. 2921-2929, 2022.